Numerical Analysis of Terahertz Emissions From an Ungated HEMT Using Full-Wave Hydrodynamic Model

Shubhendu Bhardwaj, *Student Member, IEEE*, Niru K. Nahar, *Senior Member, IEEE*, Siddharth Rajan, and John L. Volakis, *Fellow, IEEE*

Abstract—In this paper, we show how plasma-wave instability in an asymmetrically biased ungated InGaAs high-electron mobility transistor (HEMT) leads to terahertz emissions. Numerical calculations are provided using a new Maxwell-hydrodynamic solver. Using this solver, an accurate plasma-wave model is presented, accounting for nonuniform surroundings and finite dimensions of the 2D electron gas (2DEG) layer within the HEMT. We estimate that hundreds of nanowatts of power can be expected from such devices under ideal boundary conditions and sufficient channel mobility. Effects due to variations of carrier velocity, carrier concentration, and 2DEG confinement on the emitted power levels are also considered to provide design guidelines.

Index Terms—2DEG layer, high-electron mobility transistor (HEMT), instability, plasma wave, tetrahertz emission, tetrahertz power.

I. Introduction

DUE TO increasing interest in terahertz imaging, radar, and communications, terahertz sources have become an important focus in modern device research. In the search, for compact and room-temperature sources, plasma-wave electronics has provided methods for terahertz generation as an alternative to the conventional electronic and photonic methods. High-electron mobility transistors (HEMTs) (see Fig. 1) have 2-D confined electrons that can sustain plasmonic oscillations. The channel dimensions and electron carrier concentrations in these devices allow these oscillations to be in the far-infrared/terahertz frequency range. As a result, HEMTs are capable of terahertz detection and emission,

S. Bhardwaj and N. K. Nahar are with the Electroscience Laboratory, The Ohio State University, Columbus, OH 43210 USA (e-mail: bhardwaj.25@osu.edu; nahar.2@osu.edu).

S. Rajan is with the Electrical and Computer Engineering Department and the Materials Science Engineering Department, The Ohio State University, Columbus, OH 43210 USA (e-mail: rajan.21@osu.edu).

J. L. Volakis is with the Electrical and Computer Engineering Department, The Ohio State University, Columbus, OH 43210 USA, and also with the Electroscience Laboratory, The Ohio State University, Columbus, OH 43210 USA (e-mail: volakis.1@osu.edu).

Color versions of one or more of the figures in this paper are available online at http://ieeexplore.ieee.org.

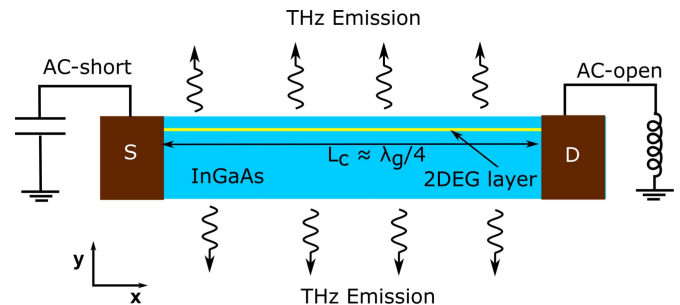Digital Object Identifier 10.1109/TED.2015.2512912

Fig. 1. Schematic of the asymmetrically biased HEMT, as proposed in [8]. Here, λ_g is the plasmon wavelength at the resonance frequency.

as experimentally shown in various reported results [1]–[6]. A mechanism for creating plasma instability, namely the Dyakonov–Shur (DS) instability, achieved by asymmetric boundary conditions at the source and drain terminals (Fig. 1) was proposed in [7] and [8]. This configuration has the potential to provide a range of terahertz devices, including mixers, detectors, and sources [9]. The concept itself is analyzed using linearized hydrodynamic model in [7]–[9]. A number of numerical studies have also been conducted to study this phenomenon, either using hydrodynamic simulations or using more rigorous Monte Carlo simulations [10]–[15]. However, these studies omit the electromagnetic (EM) wave propagation in their modeling. As a result, it is not clear how much power can be derived via emission from such a configuration.

In this paper, we show the existence of the terahertz oscillations and power emissions in such devices using full-wave hydrodynamic simulations. The method models the hydrodynamic nonlinearity in the channel, along with the field coupling to the surroundings and, therefore, accounts for the mechanism of scattering loss, reflection gain, and radiation. This enables the prediction of realistic estimates of the emitted power from the device.

Dispersion relations for plasma oscillations in infinitely large, thin 2DEG layer have been derived in [16]–[19]. These relations along with the hydrodynamic equations can be used to describe the instability in an asymmetrically biased channel [7]–[9]. However, in practice, these oscillations are further affected by the finite length and thickness of the 2DEG layer. In addition, the presence of ohmic contacts at the source and the drain also affects the oscillations. These effects are

especially significant when small channel lengths ($\approx$100 nm) and large electron densities are used and causing smaller wave confinement and stronger interaction with nonuniform HEMT surroundings. The coupled full-wave hydrodynamic solver [20], [21], [29] considers these effects for accurate HEMT performance predictions.

In Sec.-II, we first describe the coupled Maxwell-hydrodynamic solver used for simulations. This model is then validated by comparing plasma-wave dispersion curves with classically known cases. Subsequently, in Sec. III we examine the plasma-wave instability in an ungated InGaAs HEMT structure using the developed model.

II. MODELING METHOD AND VALIDATION

A. Governing Equations

The hydrodynamic approximation of the Boltzmann transport equation (BTE) provides a simple and yet accurate model of the electron transport in an HEMT channel [22]. We begin by considering the first two moments of BTE, namely particle conservation and momentum conservation equations

$$\frac{\partial n_{\mathrm{sh}}}{\partial t} + \frac{\partial j}{\partial x} = 0 \tag{1}$$

and

$$\frac{\partial j}{\partial t} + v\frac{\partial j}{\partial x} + j\frac{\partial v}{\partial x} = -\frac{qnE_x}{m_e} - \frac{j}{\tau} - \frac{KT}{m_e}\frac{\partial n_{\mathrm{sh}}}{\partial x} \tag{2}$$

where n_{sh} is the sheet carrier density, $j(=n_{\mathrm{sh}}v)$ is the sheet current, and v is the electron velocity within the 2DEG channel. E_x is the x-directed electric field along the channel (see Fig. 1), τ refers to momentum relaxation time, T is the electron temperature, and m_e is the effective electron mass. K is Boltzmann's constant, and $q = 1.6 \times 10^{-19}$ C is the charge on a single electron. Equations (1) and (2) give current density

$$\vec{J} = \frac{-q(j - j_o)}{t_{\mathrm{2DEG}}}\hat{x} \tag{3}$$

where t_{2DEG} is the thickness of the 2DEG layer. In addition, $j - j_o$ represents the ac current responsible for radiation from the channel, with j_o being the initial dc current in the channel that does not contribute to electromagnetic radiation. Maxwell's equations

$$\nabla \times \vec{H} = \frac{\partial \vec{D}}{\partial t} + \vec{J} \tag{4}$$

and

$$\nabla \times \vec{E} = -\frac{\partial \vec{B}}{\partial t} \tag{5}$$

provide the means for determining E_x in (2). Here, symbols have their usual meaning with $\vec{E} = \hat{x}E_x + \hat{y}E_y$. Note that E_x in (2) and (5) must be solved self-consistently to achieve a solution.

B. Finite-Difference Time-Domain Solution

The finite-difference time-domain (FDTD) method was chosen for solving (1)–(5). In order to achieve a self-consistent solution, a coupled FDTD solver was developed to iteratively solve both sets of equation via careful exchange of current and electric field values. We only need to model the cross sections of the device. Therefore, a 2-D FDTD solver would be sufficient. In particular, we used Yee's time-space 2-D staggered grid [23] for discretization of the device cross section. 2DEG layer was modeled using a 1-D grid of the electrons sandwiched within the dielectric.

For our numerical implementation, the center difference approximation for time derivatives was employed. The values of j and n_{sh} for the next time step were then used to solve Maxwell's equation. Space derivatives were likewise replaced by their corresponding difference equations. We noted that due to the nonlinear and highly coupled nature of advection equations, solutions could be unstable when the center difference approximation is used. Therefore, upwind difference scheme was applied to maintain the stability of the algorithm, as noted in [22]. Current $\vec{J}$ was updated into Maxwell's equations, and this process is repeated until desired simulation time was reached.

C. Solution Test and Validation

To test the validity of the presented model and its implementation, we first used it to calculate the dispersion curves for classically known cases. In particular, we consider a thin, large 2DEG layer embedded in a semiconductor (dielectric), similar to that studied in [16]. That is, an InGaAs substrate ($\epsilon_r = 13.9$) with effective electron mass $m_e = 0.042m_o$ ($m_o = 9.1 \times 10^{-31}$ kg) and electron momentum relaxation time $\tau = 1$ ps in the channel were assumed. The channel carrier density was set to $n = 10^{13}$ cm^{-2}, and the channel length was $L_c = 6$ μm large, as compared to the expected plasma wavelength in the frequency band under consideration. The thickness of the 2DEG was set to $t_{\mathrm{2DEG}} = 5$ nm. By introducing a time-harmonic E_x field, of frequency f, at the point $x = 4$ μm, a 2-D plasma wave is excited within the 2DEG channel. The same excitation process was again used for the case when the 2DEG layer is covered with a metal gate, a case analyzed in [17], with the barrier thickness $d_{\mathrm{barr}} = 38$ nm. As shown in Fig. 2(c) and (d), a plasma wave propagating away from the point of excitation was observed. The resulting propagation constant ($k = 2\pi/\lambda$) and phase velocity ($v_p = \omega/k$) are plotted in Fig. 2(a) and (b). For an ungated 2DEG layer, the dispersion relation from [16], [19], and [24] given by

$$k = \frac{1}{2a}\sqrt{\omega^4 + \frac{4a^2\omega^2\epsilon_r}{c^2}} \tag{6}$$

is also plotted. Here, $a = (n_{\mathrm{sh}}q^2/4\epsilon_o\epsilon_r m_e)$, $\epsilon_o = 8.85 \times 10^{-12}$ F/m, and ω is the angular frequency. It is seen in Fig. 2(a) and (b) that the numerical data are in agreement with (6). For the gated case, the dispersion relation is given by [17], [25]

$$k = \frac{\omega^2 m_e}{n_{\mathrm{sh}}q^2}(\epsilon_o\epsilon_r + \epsilon_o\epsilon_b \coth kd_{\mathrm{barr}}). \tag{7}$$

As known, $\epsilon_b(=\epsilon_r)$ is the dielectric constant of the barrier layer. Again, the agreement between (7) and the numerical data is quite good.
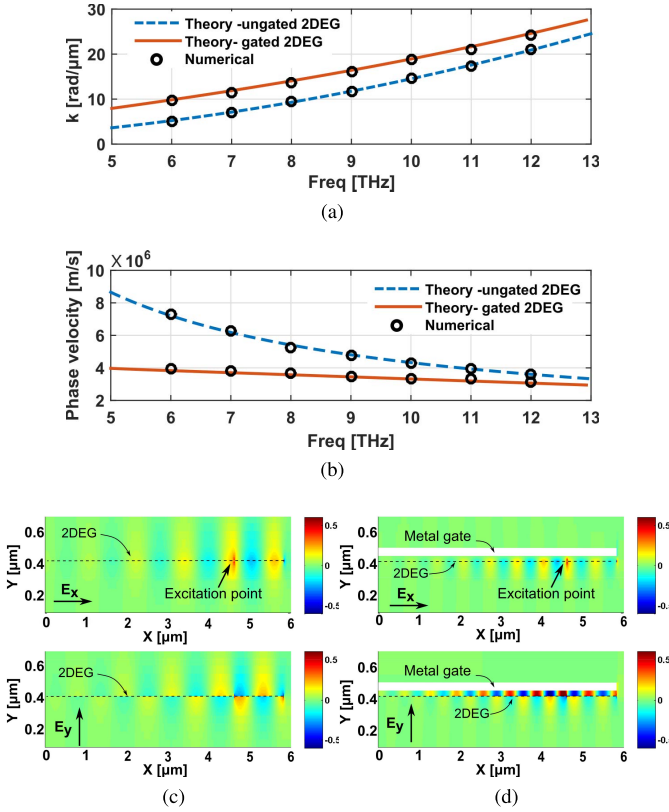
Fig. 2. Validation of the full-wave hydrodynamic model. (a) Dispersion diagrams calculated from the developed numerical model versus theoretical predictions from [16] and [17] [2DEG is in InGaAs with $\epsilon_r = 13.9$, $m_e = 0.042m_o$, and $n = 1 \times 10^{13}$ cm^{-2}, for the gated case, $d_{barr} = 38$ nm and $\mu_n = 10\,000$ cm^2/(V·s)]. (b) Phase velocity comparison from two methods for gated and ungated cases. (c) Electric field distribution (in volt per meter) due to plasma propagation in an ungated 2DEG layer. (d) Electric field distribution (in volt per meter) due to plasma propagation in a gated 2DEG layer.

We observe that for the gated case, there is strong E_y field and much weaker E_x field between the gate and the 2DEG layer [refer field plots in Fig. 2(d)]. This is especially true for small d_{barr}, i.e., $kd_{barr} \ll 1$. In such cases, the 2DEG and gate system act like a parallel plate waveguide, supporting a TEM mode. Therefore, due to this field profile, we expect a linear relation between the frequency ω and the propagation constant k, a characteristic of the TEM mode propagation. Indeed, for $kd_{barr} \ll 1$, (7) reduces to $k = \omega((m_e \epsilon_b \epsilon_o / n_{sh} q^2 d_{barr}))^{1/2}$, verifying this linear relation.

III. DYAKANOV–SHUR INSTABILITY

After validation of the developed model, we next used it to examine the DS instability in a finite length of ungated 2DEG layer in an InGaAs HEMT structure. The device, shown in Fig. 4(a), consists of a 2DEG layer ($t_{2DEG} = 5$ nm) terminated by a perfect electrical conductor (PEC) source and a drain terminal. We chose $m_e = 0.042m_o$, $\tau = 1$ ps, and a uniform carrier concentration n_{sh} in the channel. To understand the phenomenology, we assumed uniform velocity, similar to analysis presented in [7]–[9], given by $v_o = -\tau q V_{ds}/L_c m_e$, where L_c is the channel length and V_{ds} is the applied source-to-drain voltage. To implement the asymmetric boundary conditions, we fixed the ac current at (D) terminal using
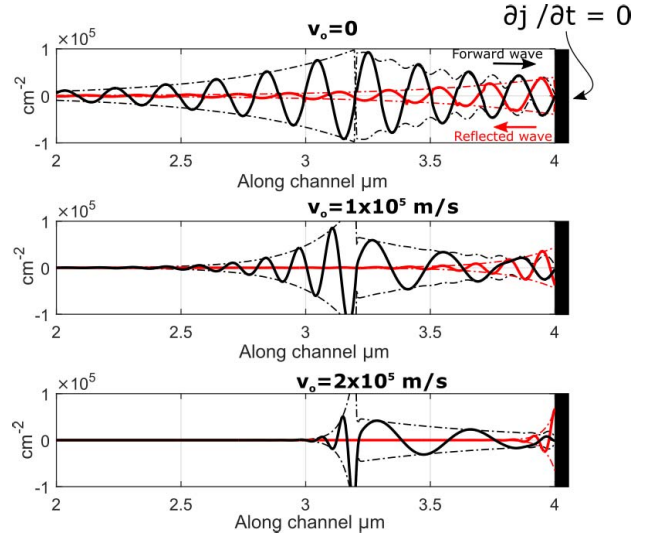

Fig. 3. Numerical modeling of wave propagation in the 2DEG terminated by ac-open conditions. Black curves: forward/backward waves. Red curves: reflected waves. Dashed-dotted curves: envelop of the fluctuations. The parameters used are $n_{sh} = 1 \times 10^{12}$, $\tau = 1$ ps, $\epsilon_r = 13.9$, and $m_e = 0.042\, m_o$. The drift velocity v_o is toward the right.

$j_{(x=L_c)} = v_o n_{sh}$, thus emulating an ac open-circuit boundary. In practice, this is equivalent of having a large inductor connected to D or having a constant current source. At the source terminal (S, $x = 0$), we used the Nuemann boundary condition ($\partial V/\partial t) = 0$ and ($\partial V/\partial x) = 0$. These enable an ac short and are equivalent to having a large capacitor or constant voltage source. To keep the terminals charge neutral, the boundary conditions $n_{(x=0)} = n_{(x=L_c)} = n_{sh}$ were also used. We note that for the FDTD model, we used the perfectly matched layer (PML), placed on all four sides of the device, to truncate the numerical grid. An estimation of the power radiated by the device was conducted by integrating the fields over the defined boundary line between the PML and the device. In particular, we have

$$P_{rad} = \int_C \frac{1}{2} \text{Re}(\vec{E} \times \vec{H}^*) \cdot d\hat{l} \qquad (8)$$

where boundary C is noted in Fig. 3(a). Here, $\hat{dl}$ is unit vector normal to boundary C with $|\hat{dl}|$ being incremental distance along C. As usual, $\vec{E}$ and $\vec{H}$ are the complex fields obtained from the Fourier transform of recorded time domain fields.

A. Instability Mechanism

Before examining the instability and radiation from an HEMT, we first consider the gain mechanism within the channel. As shown in [7], gain is a result of the open-ac boundary condition at the drain and large electron velocities due to the applied drain-to-source bias. In particular, when a plasmonic wave riding along the electron drift encounters, an ac-open boundary condition, it experiences reflective gain. That is, the amplitude of the reflected wave becomes larger than that of the incident wave. This is numerically shown in Fig. 3, where a 4-μm-long channel is considered with open boundary conditions enforced at the end ($x = 4$ μm).

The excitation is a time-harmonic field at $x = 3.15$ μm, leading to density fluctuations to propagate in the forward (right) and the backward (left) directions (shown in black curves). The reflected wave (shown in red curves) is also plotted. The respective envelopes (maximum amplitude at each point) are shown in the dashed-dotted curves. We observe that for nonzero drift velocity, the reflected wave at the drain shows increased amplitude, as compared to the incident wave. As the electron drift velocity increases, the reflective gain continues to increase as well.

Sec. III A explains how an open-ac boundary condition can lead to wave amplification. Of course, competing loss mechanism also exists due to channel scattering. Furthermore, the ac-short boundary conditions (at the source) cause reflection without amplification. Thus, for a finite-length 2DEG channel, a small fluctuation may travel between the source and the drain and amplify in each trip. At a certain frequency, such fluctuations would interfere constructively, leading to sustained oscillations.

B. Instability in Ungated InGaAs HEMT

Having examined the gain mechanism, we next model HEMT consisting of an InGaAs-based heterostructure. Using our numerical model, we consider the case when $v_o = 10^5$ m/s and $n_{sh} = 10^{12}$ cm^{-2}, with channel lengths of $L_c = 1$ μm, 500 nm, and 100 nm. To start the instability, the channel was excited by introducing a square 0.1-ps-long voltage pulse with the amplitude of 1 μV at the drain terminal, D. We note that pulse magnitude itself does not effect the final oscillation amplitude. That is, the oscillation amplitude remains the same no matter how the excitation is introduced. In practice, this excitation can come from the ambient noise itself (similar to any other oscillator). After excitation, we proceeded to record the current, observed at the drain terminal as a function of time, as plotted in Fig. 4(b) and (c). We observe that due to the plasma-wave propagation from D to S and its reflection from S, current oscillations build up near D, as shown in Fig. 4(b). For large L_c (=1 μm, 500 nm), the power loss due to the channel scattering and radiation is greater than the gain due asymmetrical source termination, causing decaying current oscillations. In contrast, for the $L_c = 100$ nm case, the scattering losses are reduced, due to shorter propagation distance. This causes a net gain in each round trip of the wave, leading to instability. Note that, in such a case, the oscillations do not amplify infinitely, rather saturate at a certain amplitude. This is due to the nonlinearity of the channel hydrodynamics, which balances the current growth with increased propagation losses as the current amplitude increases.

In other words, for $L_c = 100$ nm, the condition $2v_o/L_c > 1/\tau$ is satisfied, and oscillations are supported, as suggested in [8]. For $v_o = 2 \times 10^5$ m/s [Fig. 3(c)], we again observe oscillations. However, this time, oscillations can be sustained for $L_c = 500$ nm or smaller ($2v_o/L_c > 0.8$ ps). Thus, finite substrate dimensions and presence of ohmic contacts alter the condition of instability, making it more relaxed (e.g., velocity may be slightly smaller or channel length larger), as compared to that proposed in [8].
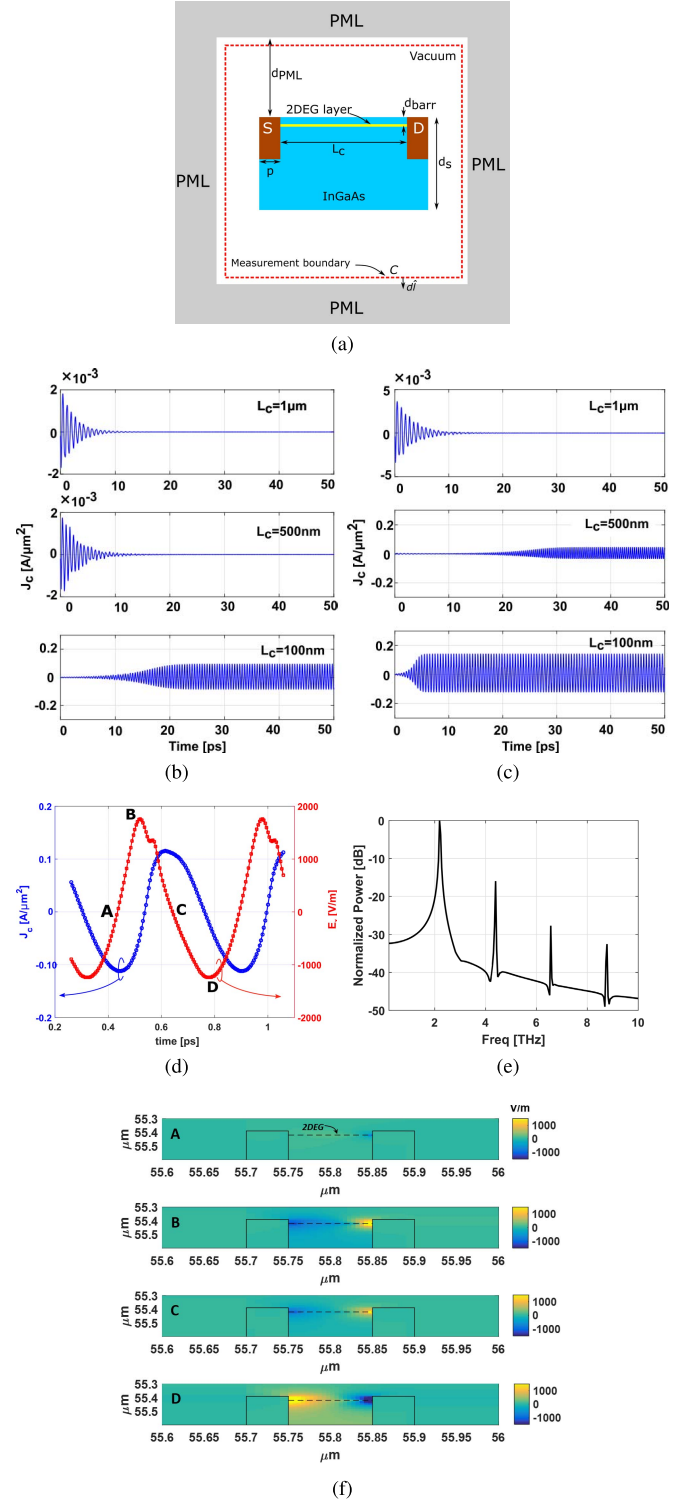

Fig. 4. Modeling of DS-instability in InGaAs HEMT. (a) Schematic used to model the HEMT (not to scale), $d_{barr} = 22$ nm, $d_S = 1.5$ μm, $p = 50$ nm, and $d_{PML} = 5$ μm. (b) Current density with time as recorded at D for varying L_c ($v_o = 1 \times 10^5$ m/s). (c) Current density with time as recorded at D for varying L_c ($v_o = 2 \times 10^5$ m/s). (d) AC-current and ac-field variation in the channel near the S terminal during one frequency cycle. (e) Corresponding radiation spectra as recorded at the measurement boundary. (f) 2-D electric fields (E_x component) associated with phase points A, B, C, and D in (d).

Fig. 4(d) shows the channel-current and channel-field variations near the terminal S during one frequency cycle (we considered $n_{sh} = 1 \times 10^{12}$ cm^{-2}, $L_c = 100$ nm,
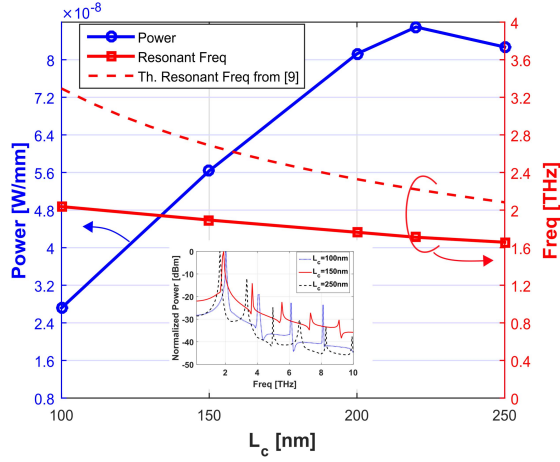
Fig. 5. Frequency and power dependence on channel length, L_c ($n_{sh} = 1 \times 10^{12}$ cm^{-2} and $v_o = 2 \times 10^5$ m/s). Theoretical calculations as per [8].

Fig. 6. Frequency and power dependence on channel carrier density, n_{sh}, in the 2DEG layer ($L_c = 100$ nm and $v_o = 2 \times 10^5$ m/s). Theoretical calculations as per [8].

and $v_o = 1 \times 10^5$ m/s for these plots). At the steady state, 2-D E-field distribution for phase points A, B, C, and D is also shown in Fig. 4(f). The plots show that the channel radiates as a leaky cavity. That is, EM waves in the vicinity of the channel interact (via reflection and diffraction) with the ohmic contacts and radiates. Therefore, the structure inherently allows for the free-space coupling of plasmonic waves. Such coupling is usually achieved using grating-gate couplers [6], [21].

Thus, sustained current oscillations in the channel act as a terahertz emitter. This power is determined using (8), as shown in Fig. 4(e). Furthermore, spectra of emissions for different cases described earlier are plotted in Fig. 5 (inset). As expected, the resonance frequencies decrease with increasing L_c. The resonance frequencies and corresponding power levels with changing L_c are plotted in Fig. 5. We note that calculated resonant frequencies are smaller than that predicted from the theoretical analysis in [8]. This implies that the resonance occurs at larger 2DEG lengths than expected quarter wavelengths. Likely reason is that the fringing fields spread well outside the channel dimensions.

We observe that most of the power is radiated at the fundamental resonance frequency, with a decrease of 20 dB or more at higher resonances. Tens of nanowatts of power can be expected from a millimeter wide device with $n_{sh} = 10^{12}$ cm^{-2} and $v_o = 2 \times 10^5$ m/s (Fig. 5). We also observe that, although the amplitude of the channel current decreases with increasing L_c, the total radiated power is increased. This is because longer L_c enables larger radiating area, and therefore an increase in the radiated power.

Fig. 5 shows the effect of changing the electron carrier concentration in the channel on the frequency and power in the radiated signal. Of course, the resonance frequency increases with increasing electron concentration and is confirmed in Fig. 6. Again, we observe that due to the presence of ohmic contacts, finite dimensions of the channel predicted plasma resonances are significantly different from those calculated using the analytical model. In addition, the power of the radiated field increases (with near quadratic dependence)
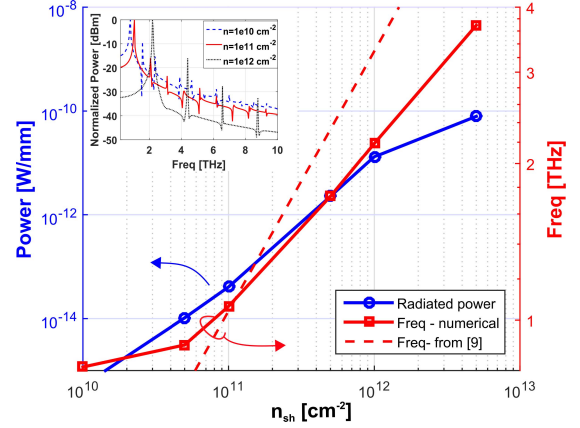
TABLE I
RADIATED POWER WITH CHANGING CARRIER VELOCITY v_o
($L_c = 100$ nm AND $n_{sh} = 10^{12}$ cm^{-2})

$v_o(m/s)$	10^5	2×10^5	3×10^5	4×10^5
$P_{rad}(\mu W/mm)$	0.013	0.027	0.032	0.033

TABLE II
RADIATED POWER WITH CHANGING 2DEG CONFINEMENT t_{2DEG}
($L_c = 100$ nm, $v_o = 10^5$ m/s, AND $n_{sh} = 10^{12}$ cm^{-2})

t_{2DEG} (nm)	5	8	12	16	20
$P_{rad}(\mu W/mm)$	0.013	0.013	0.013	0.013	0.01236

with the increase in the carrier concentration. This is attributed to an increase in the current density of the channel. Indeed, the analysis shows that as large as 0.5 μW of power can be expected from this type device.

Our simulations also reveal that the resonant frequency is not a strong function of electron drift velocity or the thickness of the 2DEG layer, although the emitted power is indeed a function of these parameters. Tables I and II describe the corresponding trends. With increasing drift velocity, we also notice increase in the radiated power. This is again expected, since current amplification is larger at higher velocities [8]. Finally, radiated power is decreasing with increasing 2DEG thickness, although this effect is rather small (Table II).

C. Effects of Velocity Saturation and Reduced Mobility

So far, we have simplified our model by assuming a linear relationship between the channel E-field and the electron velocity. Thus, at the steady state, the oscillation amplitude is limited by the nonlinearity in the channel, rather than by the velocity-saturation effect. In this section, we consider this effect, by introducing a velocity saturation at high fields. We further include the effect of reduced momentum relaxation times, since $\tau = 1$ ps can only be observed at cryogenic temperatures [26], [27]. Here, we consider these effects in our simulations. In accordance with [28], we have used saturation velocity at $v_o = 1.2 \times 10^7$ cm/s.
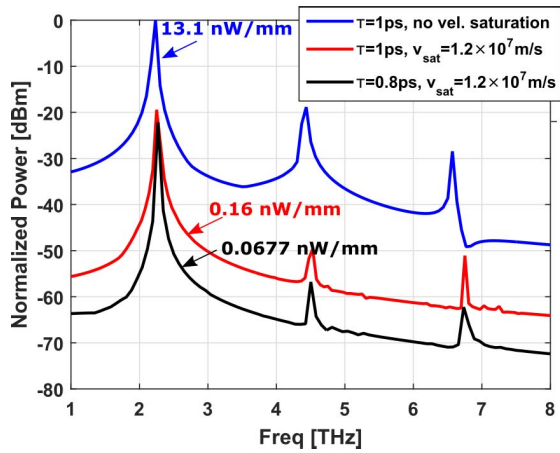
Fig. 7. Effect of velocity saturation and decreased mobility on the emitted power from the device. The considered case is for $L_c = 100$ nm and $n_{sh} = 1 \times 10^{12}$ cm^{-2}.

Fig. 7 shows the effect of velocity saturation and decreased relaxation time on the emitted power. We consider two cases: 1) velocity-saturation effect and 2) velocity-saturation effect combined with the decrease in the relaxation time. In both the cases, the power emitted at fundamental resonance frequency is decreased. In the former case, we observe a 12-dB drop in the power due to clipping of the velocity amplitude in the channel. In the latter case, the emitted power further decreases by 10 dB. This is due to increased scattering losses in the channel. We also note that for $\tau < 0.8$ ps, oscillations were not sustained due to excessive scattering losses. Therefore, no emitted power was observed for $\tau < 0.8$ ps. This leads to the conclusion that, this phenomenon should be expected at cryogenic temperatures only.

IV. CONCLUSION

Using a coupled full-wave numerical model, we have shown that the asymmetrical boundary conditions in HEMTs can cause a plasma-wave instability, leading to terahertz emissions. This numerical model contained the interaction between the 2DEG plasma waves and the surrounding fields, accounting for nonuniform media and finite dimensions of the device. Our model was used to predict: 1) more accurate plasma resonance threshold conditions; 2) accurate resonance frequency for a given set of channel parameters; and 3) maximum achievable power emissions from such devices.

REFERENCES

[1] W. Knap, Y. Deng, S. Rumyantsev, and M. S. Shur, "Resonant detection of subterahertz and terahertz radiation by plasma waves in submicron field-effect transistors," *Appl. Phys. Lett.*, vol. 81, no. 24, p. 4637, 2002.

[2] A. El Fatimy *et al.*, "Resonant and voltage-tunable terahertz detection in InGaAs/InP nanometer transistors," *Appl. Phys. Lett.*, vol. 89, no. 13, pp. 131926-1–131926-3, Sep. 2006.

[3] X. G. Peralta *et al.*, "Terahertz photoconductivity and plasmon modes in double-quantum-well field-effect transistors," *Appl. Phys. Lett.*, vol. 81, no. 9, p. 1627, 2002.

[4] W. Knap *et al.*, "Terahertz emission by plasma waves in 60 nm gate high electron mobility transistors," *Appl. Phys. Lett.*, vol. 84, no. 13, pp. 2331–2333, Mar. 2004.

[5] J. Lusakowski *et al.*, "Voltage tuneable terahertz emission from a ballistic nanometer InGaAs/InAlAs transistor," *J. Appl. Phys.*, vol. 97, no. 6, p. 064307, 2005. [Online]. Available: http://scitation.aip.org/content/aip/journal/jap/97/6/10.1063/1.1861140

[6] M. Vosseburger *et al.*, "Emission of THz radiation from optically excited coherent plasmons in a two-dimensional electron gas," presented at the Quantum Electron. Laser Sci. Conf. (QELS), Jun. 1996, pp. 206–207.

[7] M. Dyakonov and M. Shur, "Shallow water analogy for a ballistic field effect transistor: New mechanism of plasma wave generation by dc current," *Phys. Rev. Lett.*, vol. 71, pp. 2465–2468, Oct. 1993. [Online]. Available: http://link.aps.org/doi/10.1103/PhysRevLett.71.2465

[8] M. Dyakonov and M. Shur, "Current instability and plasma waves generation in ungated two-dimensional electron layers," *Appl. Phys. Lett.*, vol. 87, no. 11, pp. 111501-1–111501-3, Sep. 2005.

[9] M. Dyakonov and M. Shur, "Detection, mixing, and frequency multiplication of terahertz radiation by two-dimensional electronic fluid," *IEEE Trans. Electron Devices*, vol. 43, no. 3, pp. 380–387, Mar. 1996.

[10] H. Marinchio *et al.*, "Hydrodynamic modeling of optically excited terahertz plasma oscillations in nanometric field effect transistors," *Appl. Phys. Lett.*, vol. 94, no. 19, p. 192109, 2009. [Online]. Available: http://scitation.aip.org/content/aip/journal/apl/94/19/10.1063/1.3137189

[11] A. P. Dmitriev, A. S. Furman, V. Y. Kachorovskii, G. G. Samsonidze, and G. G. Samsonidze, "Numerical study of the current instability in a two-dimensional electron fluid," *Phys. Rev. B*, vol. 55, pp. 10319–10325, Apr. 1997. [Online]. Available: http://link.aps.org/doi/10.1103/PhysRevB.55.10319

[12] P. Nouvel *et al.*, "Terahertz emission induced by optical beating in nanometer-length field-effect transistors," *J. Appl. Phys.*, vol. 111, no. 10, p. 103707, 2012. [Online]. Available: http://scitation.aip.org/content/aip/journal/jap/111/10/10.1063/1.4718445

[13] J.-F. Millithaler *et al.*, "Monte Carlo investigation of terahertz plasma oscillations in ultrathin layers of *n*-type In$_{0.53}$Ga$_{0.47}$As," *Appl. Phys. Lett.*, vol. 92, no. 4, p. 042113, 2008. [Online]. Available: http://scitation.aip.org/content/aip/journal/apl/92/4/10.1063/1.2837183

[14] J.-F. Millithaler *et al.*, "Transconductance characteristics and plasma oscillations in nanometric InGaAs field effect transistors," *Solid-State Electron.*, vol. 56, no. 1, pp. 116–119, 2011. [Online]. Available: http://www.sciencedirect.com/science/article/pii/S0038110110003886

[15] J. Mateos and T. Gonzalez, "Plasma enhanced terahertz rectification and noise in InGaAs HEMTs," *IEEE Trans. Terahertz Sci. Technol.*, vol. 2, no. 5, pp. 562–569, Sep. 2012.

[16] F. Stern, "Polarizability of a two-dimensional electron gas," *Phys. Rev. Lett.*, vol. 18, pp. 546–548, Apr. 1967. [Online]. Available: http://link.aps.org/doi/10.1103/PhysRevLett.18.546

[17] A. Eguiluz, T. K. Lee, J. J. Quinn, and K. W. Chiu, "Interface excitations in metal-insulator-semiconductor structures," *Phys. Rev. B*, vol. 11, pp. 4989–4993, Jun. 1975. [Online]. Available: http://link.aps.org/doi/10.1103/PhysRevB.11.4989

[18] S. J. Allen, D. C. Tsui, and R. A. Logan, "Observation of the two-dimensional plasmon in silicon inversion layers," *Phys. Rev. Lett.*, vol. 38, pp. 980–983, Apr. 1977. [Online]. Available: http://link.aps.org/doi/10.1103/PhysRevLett.38.980

[19] M. A. Khorrami, S. El-Ghazaly, S.-Q. Yu, and H. Naseem, "Terahertz plasmon amplification using two-dimensional electron-gas layers," *J. Appl. Phys.*, vol. 111, no. 9, p. 094501, 2012. [Online]. Available: http://scitation.aip.org/content/aip/journal/jap/111/9/10.1063/1.4709389

[20] M. A. Khorrami, S. El-Ghazaly, H. Naseem, and S.-Q. Yu, "Global modeling of active terahertz plasmonic devices," *IEEE Trans. Terahertz Sci. Technol.*, vol. 4, no. 1, pp. 101–109, Jan. 2014.

[21] T. Otsuji, M. Hanabe, T. Nishimura, and E. Sano, "A grating-bicoupled plasma-wave photomixer with resonant-cavity enhanced structure," *Opt. Exp.*, vol. 14, no. 11, pp. 4815–4825, May 2006. [Online]. Available: http://www.opticsexpress.org/abstract.cfm?URI=oe-14-11-4815

[22] D. Vasileska, S. M. Goodnick, and G. Klimeck, *Computational Electronics: Semiclassical and Quantum Device Modeling and Simulation*. Boca Raton, FL, USA: CRC Press, 2010.

[23] A. Taflove and S. C. Hagness, *Computational Electrodynamics: The Finite-Difference Time-Domain Method*. Norwood, MA, USA: Artech House, 2005.

[24] M. Nakayama, "Theory of surface waves coupled to surface carriers," *J. Phys. Soc. Jpn.*, vol. 36, no. 2, pp. 393–398, 1974. [Online]. Available: http://dx.doi.org/10.1143/JPSJ.36.393

[25] L. Zheng, W. L. Schaich, and A. H. MacDonald, "Theory of two-dimensional grating couplers," *Phys. Rev. B*, vol. 41, pp. 8493–8499, Apr. 1990. [Online]. Available: http://link.aps.org/doi/10.1103/PhysRevB.41.8493

[26] J. Pozela, K. Požela, V. Juciene, A. Sužiedelis, N. Zurauskiene, and A. S. Shkolnik, "Electron transport in modulation-doped InAlAs/InGaAs/InAlAs and AlGaAs/InGaAs/AlGaAs heterostructures," *Lithuanian J. Phys.*, vol. 51, no. 4, pp. 270–275, 2011.

[27] X. Wallart, B. Pinsard, and F. Mollot, "High-mobility InGaAs/InAlAs pseudomorphic heterostructures on InP (001)," *J. Appl. Phys.*, vol. 97, no. 5, p. 053706, 2005. [Online]. Available: http://scitation.aip.org/content/aip/journal/jap/97/5/10.1063/1.1858871

[28] T. Akazaki, K. Arai, T. Enoki, and Y. Ishii, "Improved InAlAs/InGaAs HEMT characteristics by inserting an InAs layer into the InGaAs channel," *IEEE Electron Device Lett.*, vol. 13, no. 6, pp. 325–327, Jun. 1992.

[29] S. Bhardwaj, B. Sensale-Rodriguez, H. G. Xing, S. Rajan, and J. L. Volakis, "Resonant tunneling assisted propagation and amplification of plasmons in high electron mobility transistors," *J. Appl. Phys.*, vol. 119, no. 1, 2016.

Siddharth Rajan received the B.S. degrees in physics and electrical engineering from the Birla Institute of Technology and Science, Pilani, India, in 2001, and the M.S. and Ph.D. degrees in electrical and computer engineering from the University of California at Santa Barbara, Santa Barbara, CA, USA, in 2004 and 2006, respectively.

He is currently an Assistant Professor with The Ohio State University, Columbus, OH, USA.

Shubhendu Bhardwaj (S'12) received the B.Tech. (*summa cum laude*) degree in electronics engineering from the Indian School of Mines University, Dhanbad, India, in 2008, and the M.S. degree from the University of California at Los Angeles, Los Angeles, CA, USA, in 2012. He is currently pursuing the Ph.D. degree with The Ohio State University, Columbus, OH, USA.
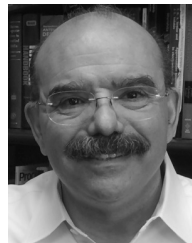
Niru K. Nahar (S'04–M'08–SM'14) received the B.Sc. (Hons.) degree in physics from Dhaka University, Dhaka, Bangladesh, the M.S. degree in physics from the Indiana University of Pennsylvania, Indiana, PA, USA, and the M.S. and Ph.D. degrees in electrical and computer engineering from The Ohio State University, Columbus, OH, USA, in 2002 and 2008, respectively.

She is currently a Research Scientist with The Ohio State University.

John L. Volakis (S'77–M'82–SM'89–F'96) was born in Chios, Greece, in 1956. He received the B.E. (*summa cum laude*) degree from Youngstown State University, Youngstown, OH, USA, and the M.Sc. and Ph.D. degrees from The Ohio State University, Columbus, OH, USA, in 1979 and 1982, respectively.

He has been the Roy and Lois Chope Chair Professor of Engineering with The Ohio State University since 2003.